Sensor and Simulation Notes

Note 547

October 2009

An Iterative Search Algorithm for Designing Bends in Electromagnetic Structures

Naga R. Devarapalli, Carl E. Baum, Christos G. Christodoulou, Edl Schamiloglu

University of New Mexico, Albuquerque, NM 87131, USA

ABSTRACT

A design approach to obtain the function defining a bend, called the H-plane taper, that minimizes the reflected power at the input of a structure, called the H-plane-bend-radiator, is presented. Note that the H-plane-bend-radiator (HPB-radiator) is used as part of a high power antenna and therefore the requirement for a smooth taper function containing no sharp corners is apparent. The smoothness requirement on the H-plane taper function increases the possible number of functions to be considered in search of a solution, thereby increasing the complexity of the problem. It is hypothesized that the general design philosophies in the approach can be adopted as a basis for designing other structures with bends similar to the H-plane taper in the HPB-radiator.

I. INTRODUCTION

It is assumed that the HPB-radiator's feed-waveguide only supports the TE_{10} mode, the dominant mode in a rectangular waveguide. The HPB-radiator shown in Fig. 1 is an H-plane bend terminating in a radiating aperture with the narrow dimension of the waveguide flaring out to the maximum possible width; the maximum possible width is the same as the maximum dimension of the narrow wall of a rectangular waveguide that still only supports the TE_{10} mode. The following parameters influence the reflected power at the feed-guide of the HPB-radiator: the radiating aperture's dimensions, the H-plane taper function and the relative locations where the aperture and H-plane taper begin. This work presents a new approach for designing the H-plane taper function of the HPB-radiator when the other parameters that influence the reflected power at the feed-guide are kept constant.

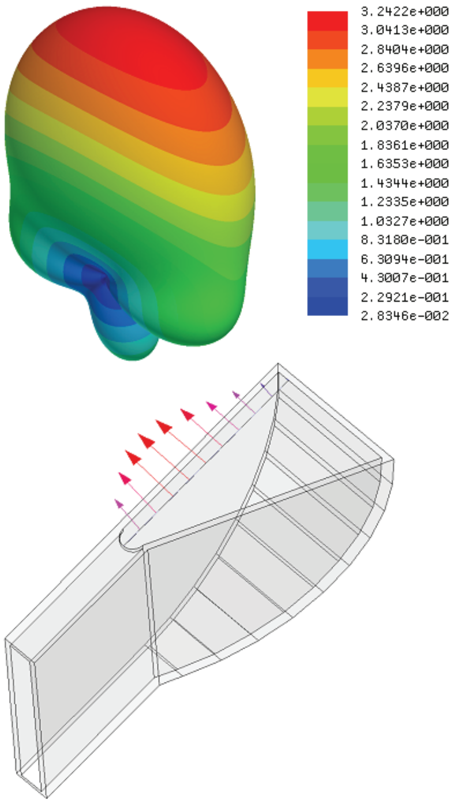

Fig. 1. H-plane-bend-radiator along with its aperture E-field distribution and the 3-D radiation power pattern in absolute units. Note that all of the input energy at the feed-waveguide is assumed to be in the dominant mode.

The radiation patterns of the HPB-radiator and a magnetic dipole into a half-space are similar. The HPB-radiator is used as the standard element of the high power antenna array shown in Fig. 2. Owing to its split-waveguide input, the array has the capability to beam steer. Each split in the waveguide terminates in an identical HPB-radiator element as shown in Fig. 2. The inter-element spacing of the array is optimized to maximize the directivity of its fan-beam radiation pattern. Minimizing the reflected power at the inputs of the identical HPB-radiator elements minimizes the reflected power at the input of the array. The array's radiated electric (E-) fields are strongly linearly polarized in the direction of the broad dimension of its fan-beam radiation pattern. The initial idea for the arrangement of the elements of the array was obtained from [1] and the details of the design of the array are described in [2].

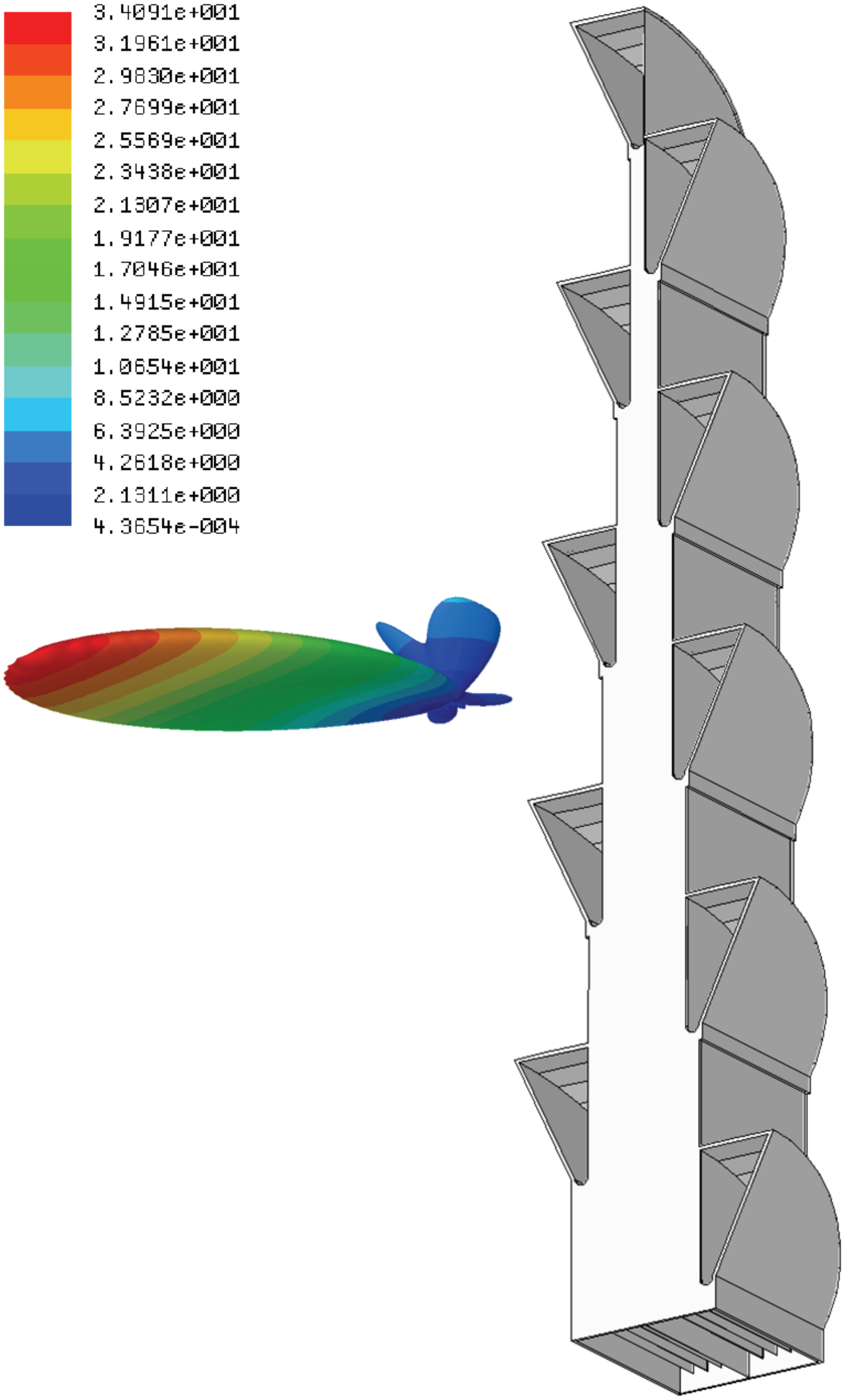

Fig. 2. High power antenna array with a split-waveguide input that uses the HPB-radiator as its standard element.

Note the following characteristics with respect to the HPB-radiator shown in Fig. 1: its aperture begins at a location along the length of the waveguide that is slightly before the beginning of the H-plane taper; the narrow wall flare does not disrupt the planar symmetry that the H-plane taper has in any plane parallel to the H-plane. The latter characteristic means that for design purposes of the HPB-radiator's H-plane taper, the HPB-radiator can be reduced to a two-dimensional structure since the narrow wall flare is known.

II. HPB-RADIATOR UNDER CONSIDERATION

The HPB-radiator under consideration in this work is a simplified version of the one shown in Fig. 1; it has no narrow-wall flare with an aperture length of a half free space wavelength and an aperture that begins at the same location along the length of the waveguide where the H-plane taper begins. The feed-guide is a standard X-band (WR-90) waveguide operating at 10GHz. The general design procedure is now presented with reference to designing the H-plane taper for the HPB-radiator just described.

The design procedure is initiated in HFSS (High Frequency Structure Simulator). Simulations were performed for an HPB-radiator whose H-plane taper function is defined by the location of a single point (HPB-radiator-1-point-optimization). Figure 3(a) shows a two-dimensional view of the HPB-radiator used in HPB-radiator-1-point-optimization, where the missing dimension is the narrow dimension of the waveguide. The data from these simulations, i.e. the point locations in the search-space (as shown in Fig. 3(a)) versus the power reflected, forms the sample data to be analyzed. The details of this analysis are presented. Figure 3(b) is a surface plot of the amplitude of the power reflected into the feed-guide for the various simulation points in the search-space of Fig. 3(a). For instance, consider the HPB-radiator whose H-plane taper function is defined by the location of the simulation point shown in Fig. 3(a). The shade of the surface plot at the corresponding location (of the above mentioned simulation point) in Fig. 3(b) represents the amplitude of the power reflected by this specific HPB-radiator.

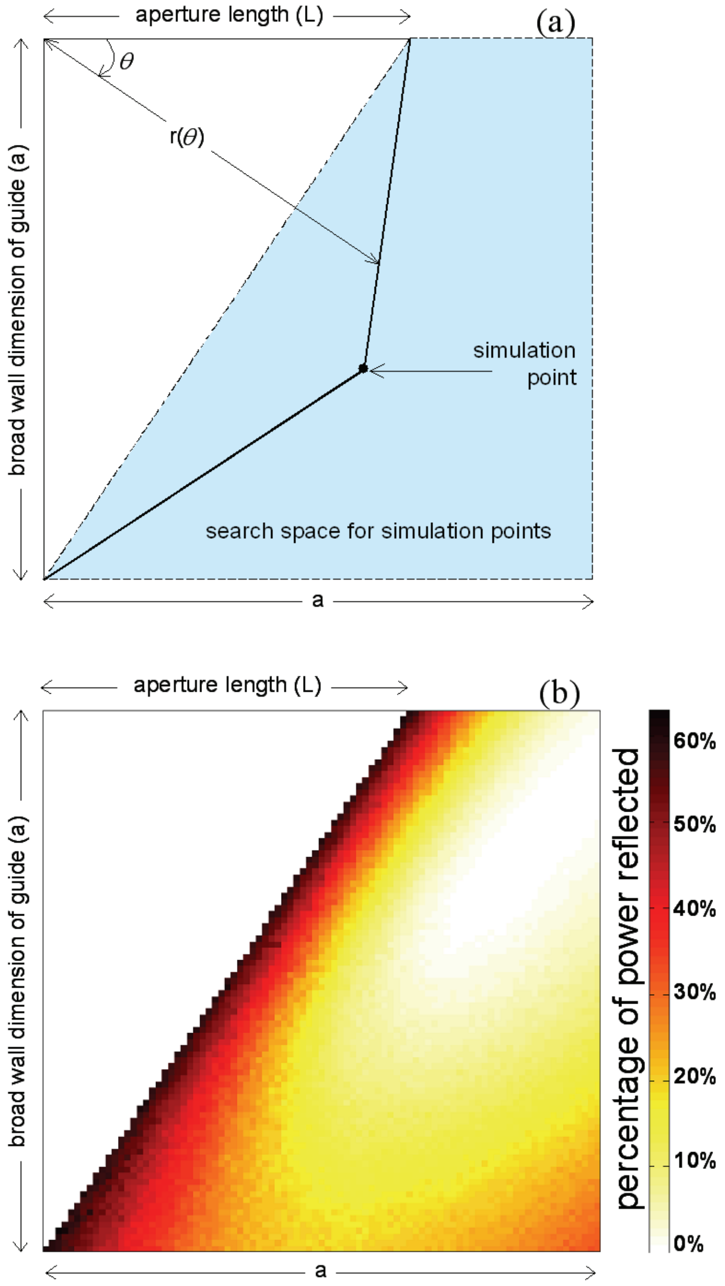

Fig. 3. (a) Illustration of the HPB-radiator in two dimensions, showing the search-space for HPB-radiator-1-point-optimization. (b) Surface plot showing the amplitudes of reflected powers for structures defined by various simulation points in the search-space shown in Fig. 3(a).

III. DIMENSIONAL OFFSET HYPOTHESIS

The design of the HPB-radiator element with a smooth H-plane taper function using just analytical or computational electromagnetics techniques felt intractable and the following novel design approach that processes the computational analysis (HPB-radiator-1-point-optimization) data using iterative search algorithms is proposed. The search algorithms were developed to utilize user-defined design criteria that can be adjusted according to the information available from the computational analysis data regarding the structure to be designed. The approach is based on the following hypothesis (called the dimensional offset hypothesis): for a fixed aperture length, the power reflected due to any taper function has a predictable dependence on the dimensional offset between the given taper function and the ideal-taper-function. The ideal-taper-function for a given aperture length produces the lowest reflected power and is represented by the smooth curve in Fig. 4. The shaded region that is represented by the dotted lines in Fig. 4 represents the dimensional offset between the ideal-taper-function and a sample taper function (represented by the discrete curve in Fig. 4 and defined completely by the location of a single point).

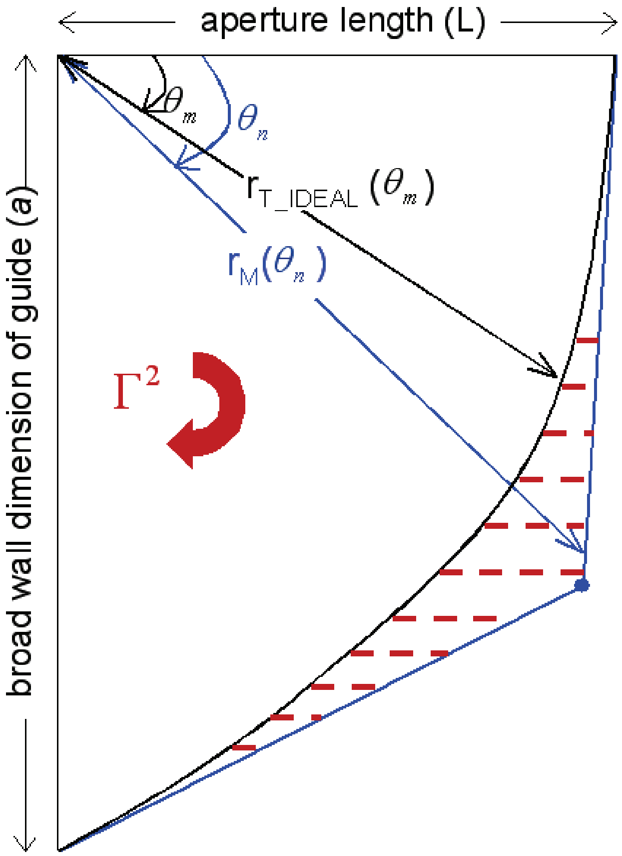

Fig. 4. Illustration for the dimensional offset hypothesis.

IV. IMPLEMENTATION OF THE DIMENSIONAL OFFSET HYPOTHESIS

To find the ideal-taper-function, the dimensional offset hypothesis is proposed to be implemented as follows. The dimensional offset is characterized by the dimensional offset parameter (p) as defined in Eq. 1. The H-plane taper functions obtained from HPB-radiator-1-point-optimization are labeled as ‘measured-taper-functions’; therefore the power reflected into the feed-waveguide by an HPB-radiator constructed using a measured-taper-function is known. The ‘test-taper-functions’ are used to eventually lead to the ideal-taper-function. The search-space for the test-taper-functions is discretized as shown in Fig. 5(a) and each possible combination of points in the discretized space leads to a test-taper-function. A test-taper-function formed by a combination of points is as shown in Fig. 5(a).

$$p = \sum_{n=2}^{N} p_n \Delta\theta_n \qquad \textbf{(1)}$$

where:

$p_n = \left| r_M(\theta_n) - r_T(\theta_n) \right| w(\theta_n)$

$r_M(\theta_n)$ is the radius of a ‘measured-taper-function’ at an angle of θ_n as shown in Fig. 4

$r_T(\theta_n)$ is the radius of a ‘test-taper-function’ at an angle of θ_n

$w(\theta_n)$ is a user defined weight function at an angle of θ_n

$\Delta\theta_n = \theta_n - \theta_{n-1}$

$\Delta\theta_n \le 1^\circ$

From Fig. 4: $\theta_1 = 0^\circ$ and $\theta_N = 90^\circ$

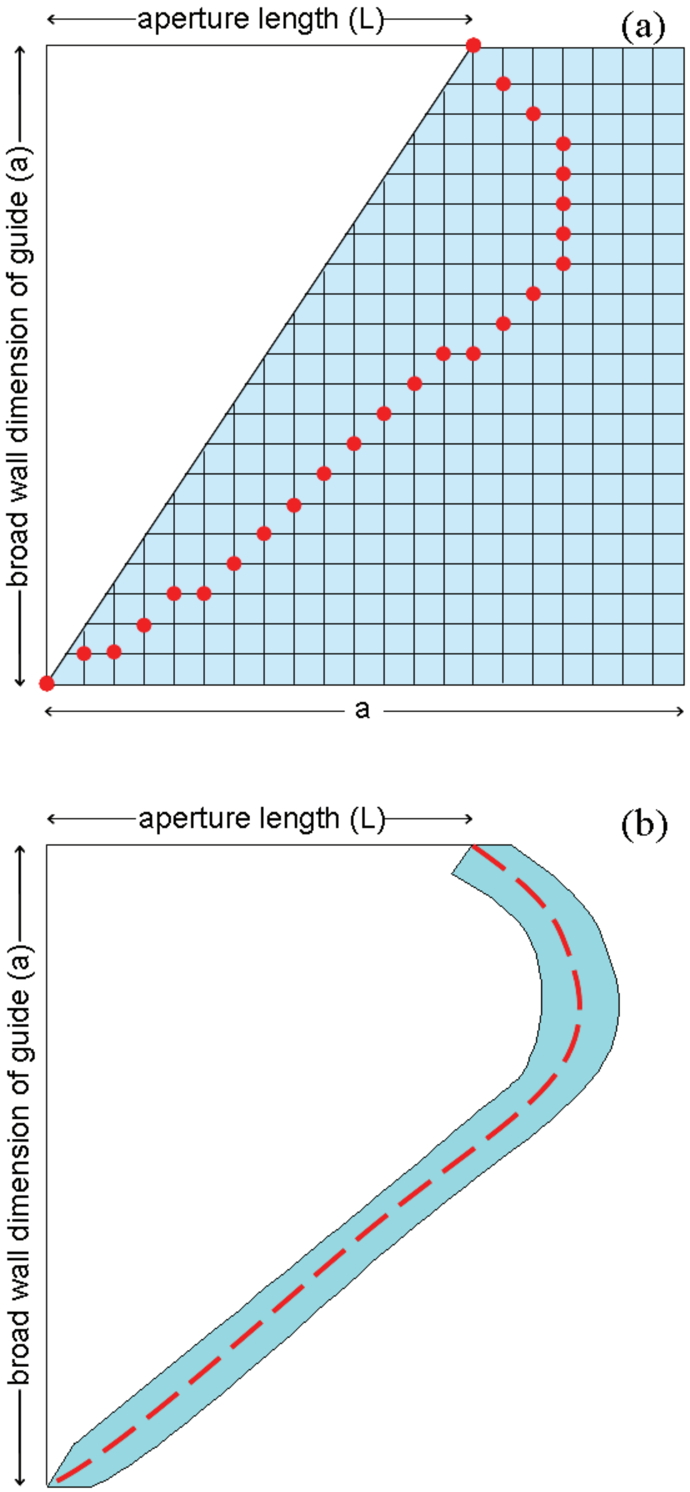

Fig. 5. Search-space (given by the shaded region) for test-taper-functions (two sample test-taper-functions are given by the dotted/dashed lines).

Consider, for instance, that there are one hundred measured-taper-functions and since for each measured-taper-function there is a corresponding reflected power measurement, there are one hundred corresponding reflected power measurements. Now consider a test-taper-function; from Eq. 1 there would be one hundred dimensional offset parameter values corresponding to the test-taper-function. Now the dimensional offset hypothesis is used as follows. A scatter plot is made between the above mentioned reflected power values and dimensional offset parameter values. When the dimensional offset's characterization is adequate, the test-taper-function that produces the scatter plot with the least scatter is the ideal-taper-function. It can be seen that the scatter plot in Fig. 6(a) has a higher scatter/fit-error compared to the scatter plot in Fig. 6(b); hence the test-taper-function used to obtain Fig. 6(b) is a better test-taper-function.

(a) Test-taper-function with higher fit-error

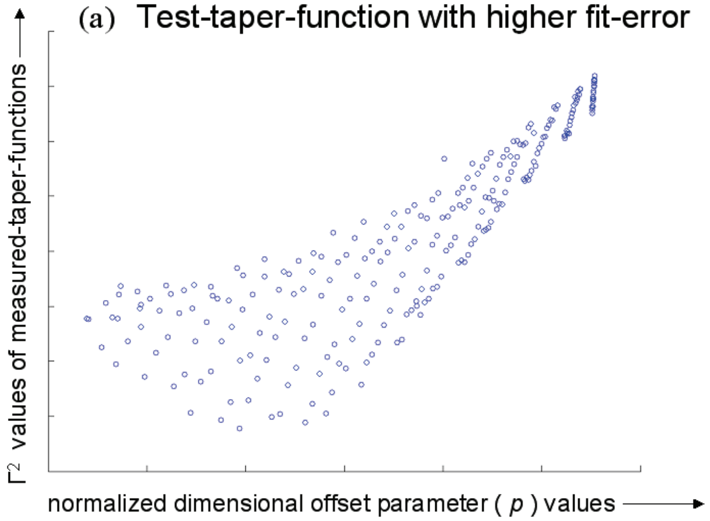

(b) Test-taper-function with lower fit-error

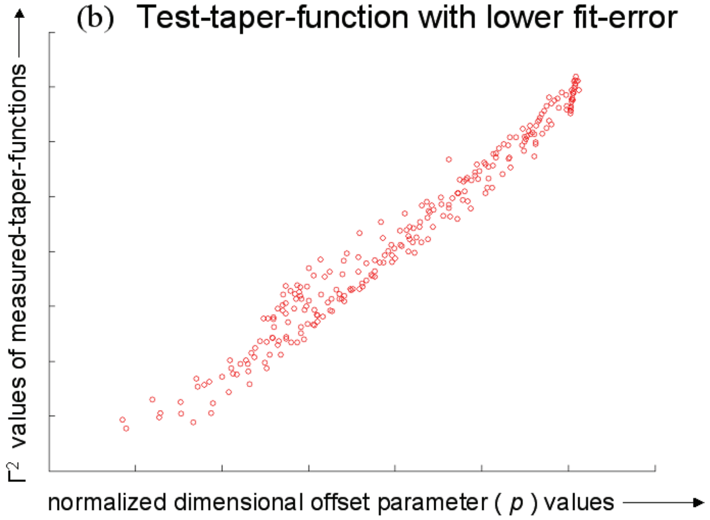

Fig. 6. (a) Scatter plot with higher scatter/fit-error. (b) Scatter plot with lower scatter/fit-error.

To make the search for the ideal-taper-function efficient, the test-taper-functions can be iterated in two stages. The first stage is shown in Fig. 5(a), where the grid used to obtain the set of points that make a certain test-taper-function, is coarse. After obtaining the best test-taper-function given the coarse grid, the search-space around this best test-taper-function is used as the new search-space as shown in Fig. 5(b). The search-space in Fig. 5(b) is discretized more finely than that in Fig. 5(a) leading to the ideal-taper-function. The coarseness of the grid in Figs. 5(a) and 5(b) is dependent upon the number of iterations that can be handled by the computational resources available. Hence for a given search-space discretization, the best test-taper-function becomes the ideal-taper-function.

To summarize, the search for the optimal HPB-radiator's ideal-taper-function is made possible by mapping the power reflected by a taper function (variable-1) to the corresponding scatter plot's fit-error (variable-2). Since the computational time required to find variable-2 is much lower compared to variable-1, it is possible to find the dimensional offset parameters and the scatter plots' fit-errors corresponding to the various test-taper-functions and these iterations eventually lead to the ideal-taper-function.

V. VERIFICATION OF THE DIMENSIONAL OFFSET HYPOTHESIS

The aim of the following discussion is to illustrate that the dimensional offset hypothesis has the potential to be used as a procedure for designing the HPB-radiator. But note that the characterization of the dimensional offset and the procedure for determining the amount of scatter in the scatter plots needs more investigation. For instance, consider the dimensional offset's characterization in Eq. 1. It is assumed that the values of the dimensional offset parameter at various angles are linearly independent of each other unless these dependencies can be factored into the characterization of the weight function at various angles. The characterizations of the weight function and the dimensional offset, therefore, need more investigation. It is also assumed that the characterization of the dimensional offset can be completely performed in polar coordinates, which also needs more investigation. The amount of scatter in the scatter plots can be determined by the fit-error resulting from fitting each scatter plot with a polynomial; more investigation is needed to determine the order of this polynomial.

It is also hypothesized that it is reasonable to make the dimensional offset hypothesis while designing other kinds of structures as long as the dimensional offset parameter's calculation and the scatter plots' analysis is appropriately performed.

The demonstration of the dimensional offset hypothesis' merit is performed in two steps that were implemented in a program coded in MATLAB (Matrix Laboratory). In the first step, the various test-taper-functions are described by Eq. 2 and are labeled as 'spiral-taper-functions'. The best test-taper-function from the first step is a spiral-taper-function with n=1; it is used in the second step, where the various test-taper-functions are described by Eq. 3 and are labeled as 'spiral-sine-taper-functions'. Figure 7 (8) shows the extent of variation for the test-taper-functions in step one (two) and the best test-taper-function obtained from this step is the curve represented by the solid line. The weight function given in Eq. 1 is chosen to be equal to unity for the entirety of this analysis. Also, to characterize the amount of scatter in the scatter plots, the following procedure is undertaken. First the data in each scatter plot is fitted to a first order polynomial. Then the fit-error for each of the scatter plots is obtained by taking the sum of the absolute values of the differences between the y-coordinates of the scattered points and the corresponding y-coordinates of the points on the fitted polynomial. The y-axis of the scatter plots corresponds to the reflected power measurements of the measured-taper-functions. So the fit-error of a certain scatter plot is used to characterize the amount of scatter in it; a higher fit-error corresponds to a higher amount of scatter.

$$r(\theta) = \frac{\mathrm{a} - \mathrm{L}}{(\pi/2)^{\mathrm{n}}}\theta^{\mathrm{n}} + \mathrm{L} \qquad \textbf{(2)}$$

where:

$0^{\circ} \leq \theta \leq 90^{\circ}$

$0.6 \leq n \leq 4$

a, L, θ, $r(\theta)$ are shown in Fig. 7

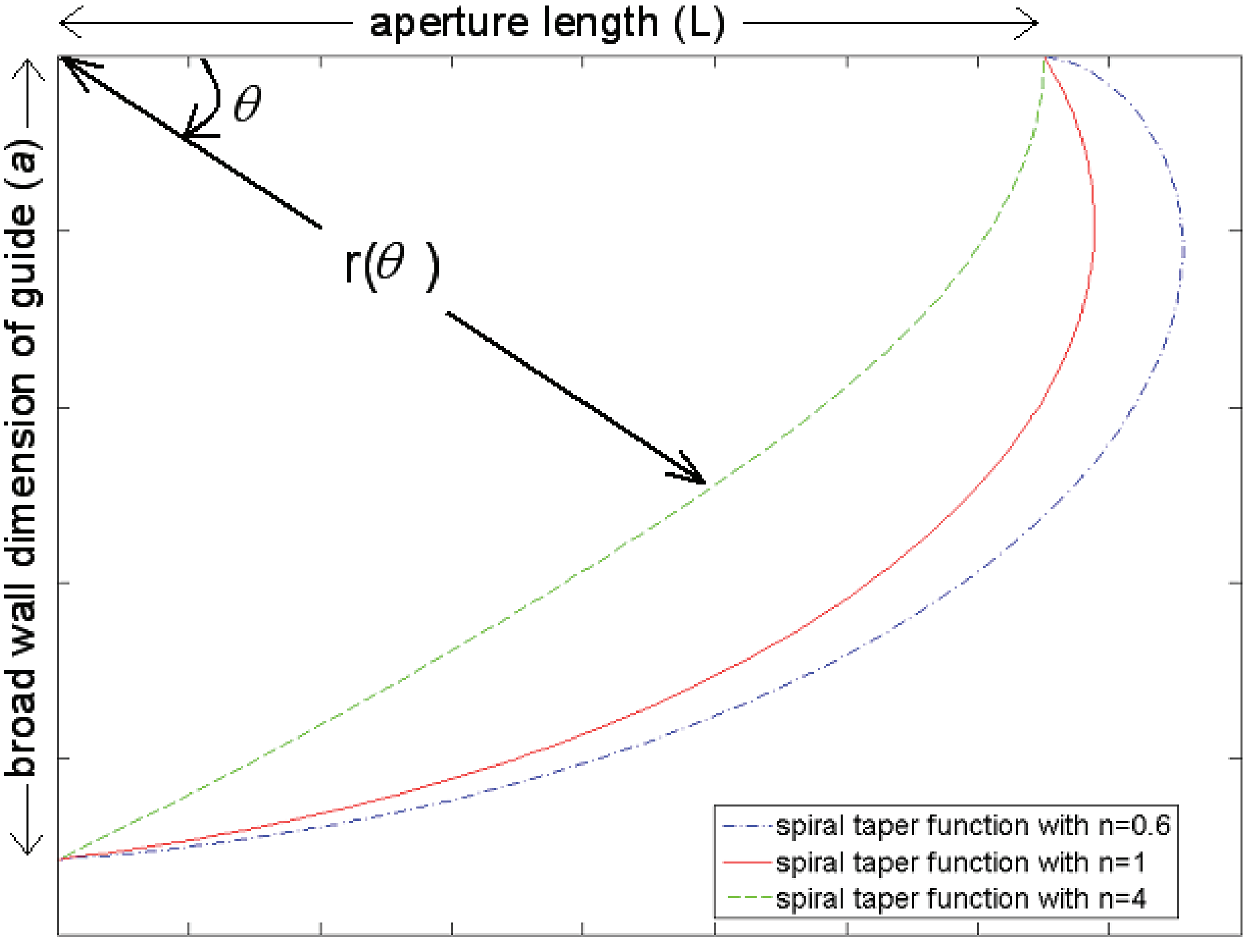

Fig. 7. Spiral-taper-functions used for testing hypothesis.

$$r(\theta) = \frac{\mathrm{a} - \mathrm{L}}{\pi/2}\theta + \mathrm{L} + (\mathrm{sine\_amp})\sin(\frac{2\pi\theta}{\pi/2}) \qquad \mathbf{(3)}$$

where:

$0^\circ \leq \theta \leq 90^\circ$

$0.1 \leq \mathrm{sine\_amp} \leq 4$

a, L, θ, $r(\theta)$ are shown in Fig. 8

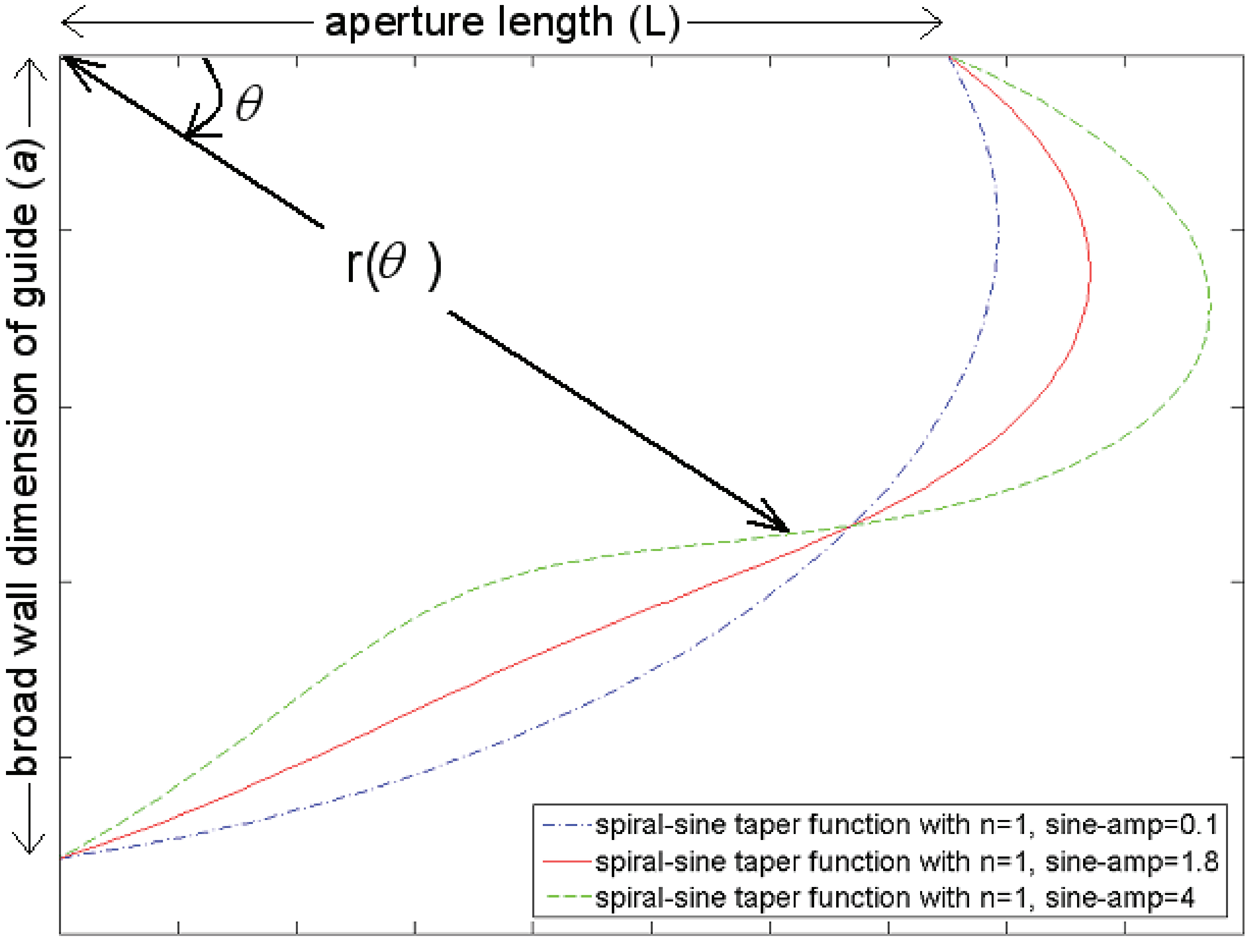

Fig. 8. Spiral-sine-taper-functions used for testing hypothesis.

Figures 9 and 10 demonstrate the merit of the dimensional offset hypothesis. Each scatter point in Fig. 9 (10) corresponds to a test-taper-function that was obtained from Eq. 2 (3). HFSS was used to find the reflected power from using each of the test-taper-functions defined by Eq. 2 (3) as the H-plane taper of the HPB-radiator. Figures 9 and 10 show a trend that a lower fit-error approximately corresponds to a lower reflected power for a test-taper-function defining the H-plane taper of the HPB-radiator.

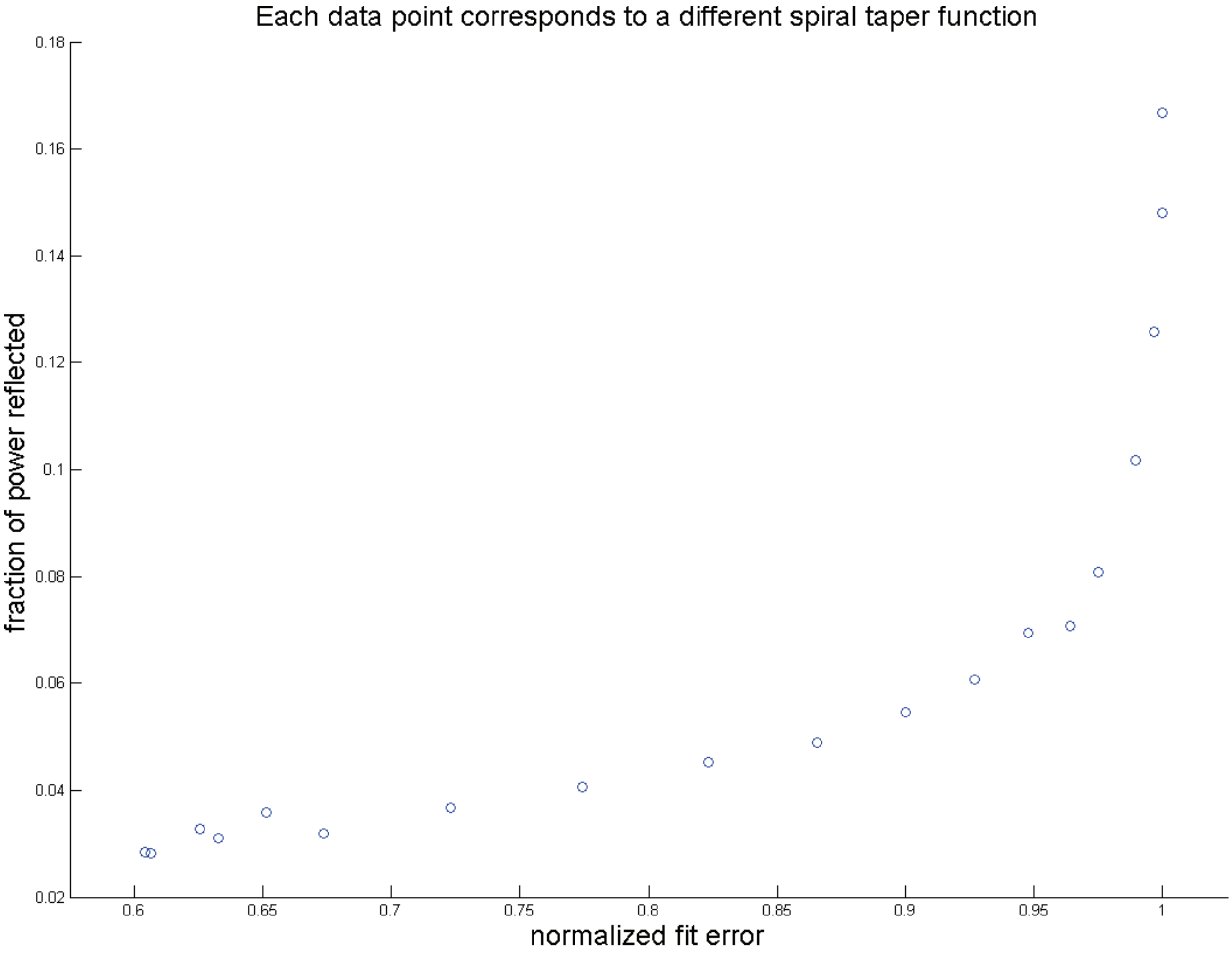

Fig. 9. Hypothesis verification for Spiral-taper-functions.

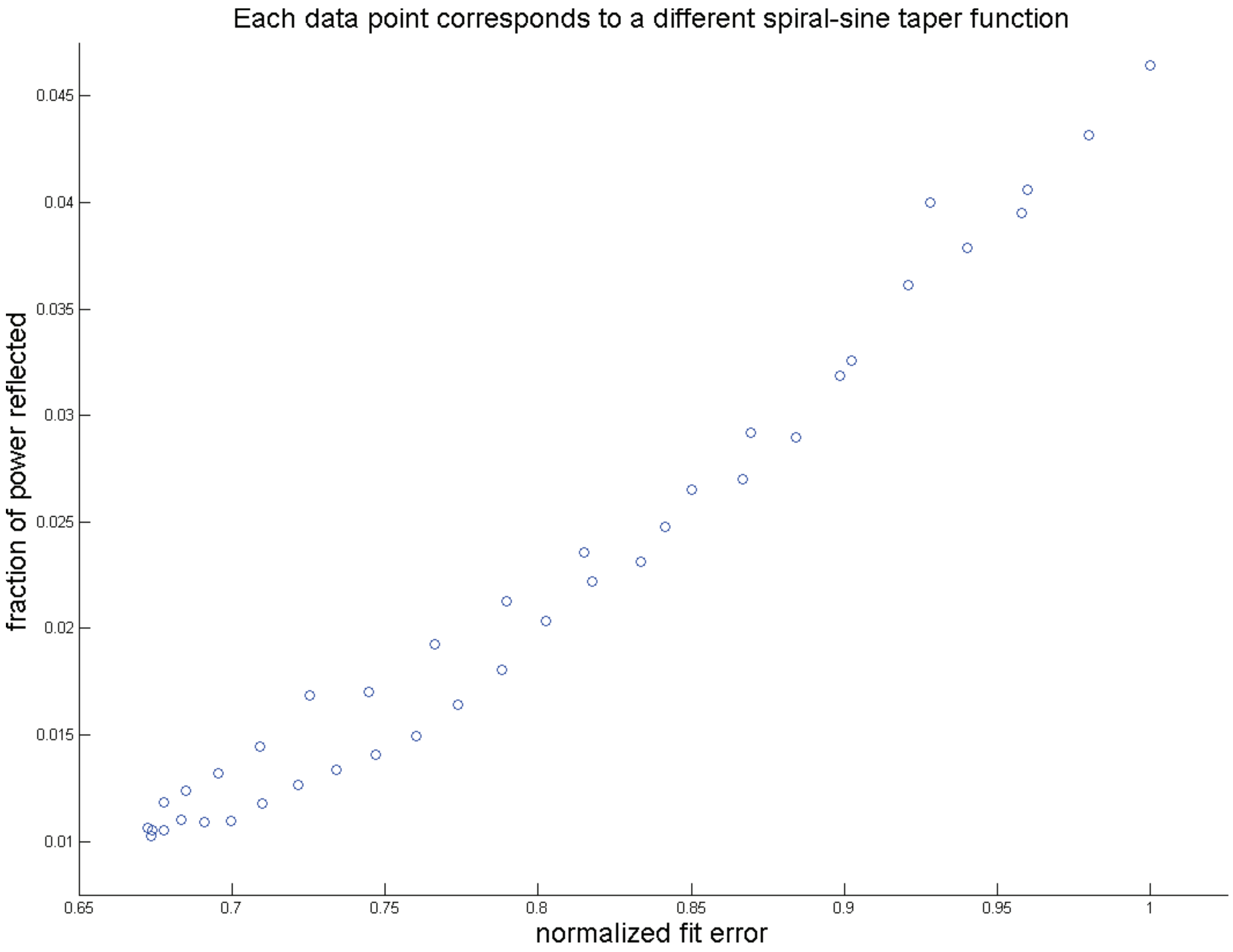

Fig. 10. Hypothesis verification for Spiral-sine-taper-functions.

VI. EXPERIMENTAL RESULTS

The analysis presented partly relies on the accuracy of the HFSS results. The objective of this section is to test the strength of an HFSS result used in the analysis, by comparing it to the corresponding experimental result. Figure 11 shows the structure of an HPB-radiator element that when simulated in HFSS would result in a data sample point that is part of the HPB-radiator-1-point-optimization. The reflection coefficient, E and H-plane radiation patterns of the HPB-radiator that are obtained from HFSS are verified experimentally. The slotted line technique [3] is used to measure the reflection coefficient of the HPB-radiator. The theoretical, experimental values of the reflection coefficient are 0.17∠-136°, 0.18∠-144° respectively. The theoretical, experimental E- (H-) plane radiation patterns are compared in Fig. 12(a) (12(b)). There is good agreement between the theoretical and experimental results.

Fig. 11. (a) Schematic of the X-band HPB-radiator for experimental verification.

(b) X-band HPB-radiator used for experimental verification.

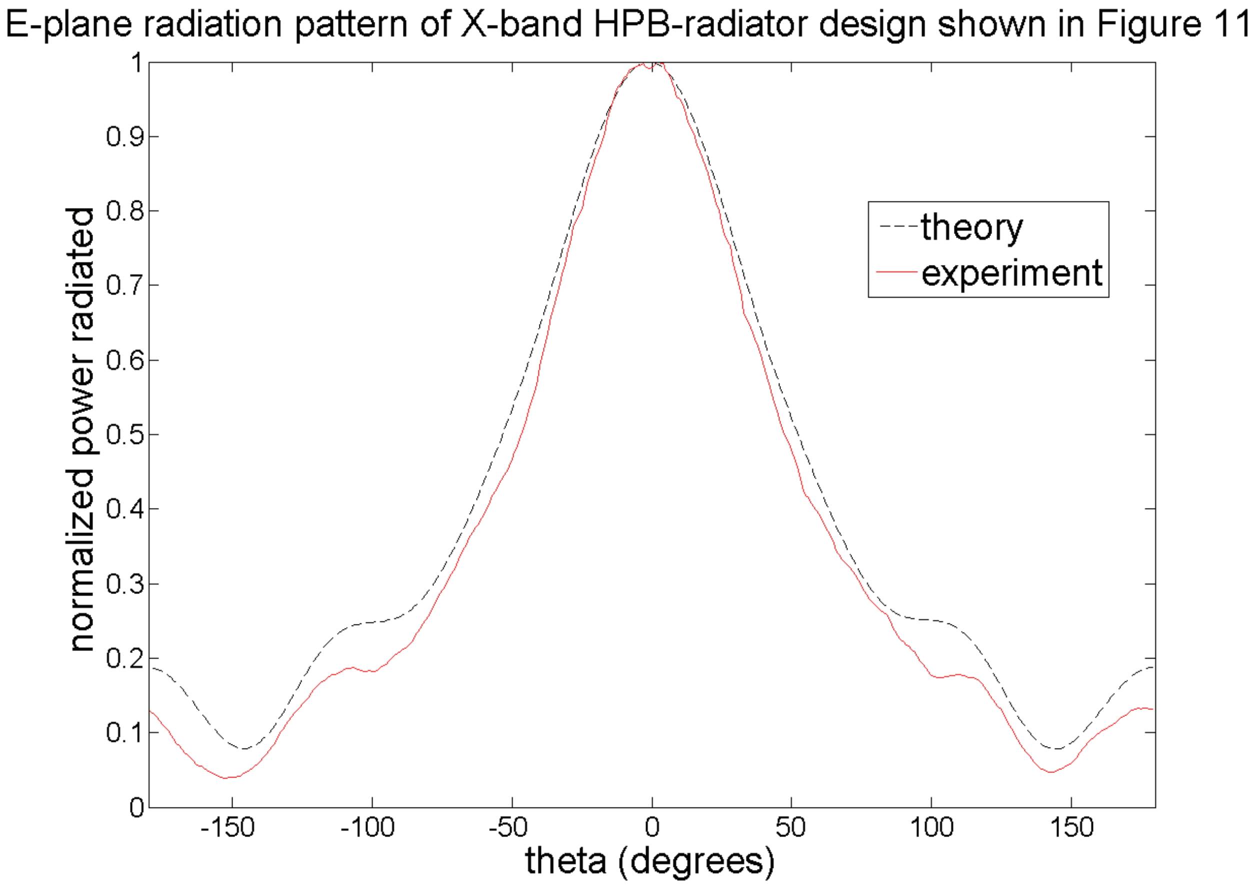

Fig. 12(a). E-plane radiation pattern of the X-band HPB-radiator shown in Fig. 11.

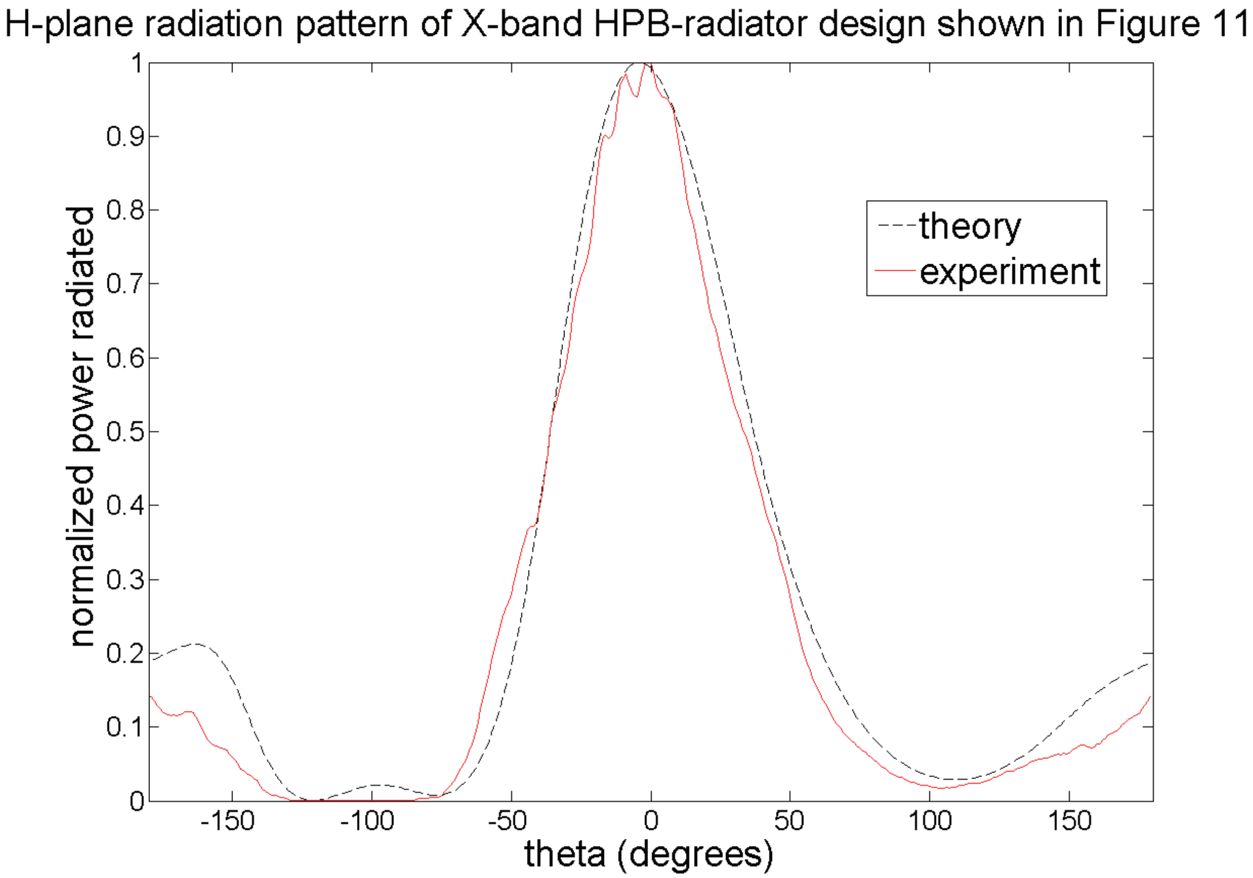

Fig. 12(b). H-plane radiation pattern of the X-band HPB-radiator shown in Fig. 11.

REFERENCES

[1] C. E. Baum; **Sidewall Waveguide Slot Antenna for High Power**; Sensor and Simulation Notes, Note 503. http://www.ece.unm.edu/summa/notes/SSN/Note503.pdf

[2] N. R. Devarapalli; "Split-waveguide-HPB-array" in **Rectangular waveguide narrow-wall longitudinal-aperture antenna arrays for high power applications**; Ph. D. thesis, University of New Mexico, Albuquerque, NM 87131, USA, pp. 61-71, August 2009.

[3] D. M. Pozar; **Microwave Engineering**; John Wiley & Sons, New York, 2005.